Application of a histogram modification algorithm to the processing of raindrop images

Nithya A. Sivasubramanian
John R. Saylor
Clemson University
Department of Mechanical Engineering
Clemson, South Carolina 29634-0921
E-mail: jrsaylor@ces.clemson.edu

Abstract. Automatic processing of digital images of falling raindrops is complicated by a less than ideal grayscale image histogram. These histograms do not display a bimodal shape and lack an easily defined minimum, making it difficult to choose a threshold for creating a binary image. To help identify peaks in these histograms, and simplify threshold selection, a histogram modification technique originally developed by Peleg is used. This method was modified slightly and then applied to raindrop image processing. Its performance is quantified. [DOI: 10.1117/1.2899101]

Subject terms: image processing; histogram modification; rain; precipitation.

Paper 070410R received May 15, 2007; revised manuscript received Oct. 27, 2007; accepted for publication Nov. 28, 2007; published online Apr. 2, 2008.

1 Introduction

The measurement of the rainfall rate over large areas is achieved primarily using precipitation radars. These are typically single polarization radars in operational weather stations, and dual polarization radars are often used in research applications.[1] Although radars provide large spatial coverage, the accuracy of measured rainfall rates are limited due to several error sources. One such source stems from the fact that the statistical distribution of raindrop size and shape must be known to accurately extract rainfall rates from radar data. Errors are introduced due to imperfect knowledge of the statistical distribution of the size and shape of raindrops.[2,3] Specifically, the raindrop size distribution (DSD) is needed. Improvements in the accuracy of rainfall estimates obtained by radars can be obtained from an improved understanding of the DSD. Theoretical models have been developed to predict the shape of raindrops,[4,5] and laboratory measurements have been carried out with drops of different sizes to understand their behavior.[6–8] However, much work remains to be done in this area, especially in obtaining field measurements of raindrop size and shape.[9]

A particularly useful method for measuring the DSD in the field is to image raindrops as they are illuminated from behind,[10,11] a method that has recently been developed by NASA in the form of the Rain Imaging System (RIS).[12] Figure 1 shows the general optical setup used in this system, where the camera records images of drops as they are backlit by a lamp, resulting in an image of the drop silhouette. A sample grayscale image of a drop obtained from this backlit configuration is shown in Fig. 2(a). A bright spot can be seen in the center of the drop, which is the image of the light source, as seen through the drop. These bright spots or "holes" in the drop image are present only when the drop resides within the depth of field of the camera, that is, it is in focus. This characteristic is useful in digital image processing of drop images because it provides an objective criterion for determining whether or not a drop is in focus.

To obtain DSDs using imagery obtained from the system illustrated in Fig. 1, the grayscale images must first be thresholded, and a determination must be made as to whether a hole exists in each raindrop image. If a hole exists, the drop is then sized. By performing this operation on a large number of raindrop images, a DSD can then be computed. Sample grayscale images of an in-focus and out-of-focus raindrop are presented in Figs. 2(a) and 2(c), respectively. Thresholded versions of these two images are presented in Figs. 2(b) and 2(d), respectively.

Saxena and Saylor[13] calculated the *dof* (depth of field) of the system shown in Fig. 1, using the following equation:

$$dof = z_e - z_s, \tag{1}$$

where z is the distance from the camera along the optical axis, and z_s and z_e are the z positions where observation of a hole "starts" and "ends," respectively. Here z increases with distance from the camera. This definition for *dof* is used in the present study as well. For images having a hole, the measured diameter D_m is computed by counting the number of pixels that fall within the drop boundary using the following equation:

$$D_m = 2\sqrt{\frac{A_d}{\pi}}, \tag{2}$$

where A_d is the area of the drop (in mm^2) and is given by

$$A_d = n_p \times 0.05 \times 0.1, \tag{3}$$

where n_p is the number of pixels falling within the drop boundary and 0.05 and 0.1 are the pixel resolutions (mm/pixel) used in this work for the x and y directions, respectively. Note that A_d includes all pixels inside the drop boundary, including pixels comprising the hole.

0091-3286/2008/$25.00

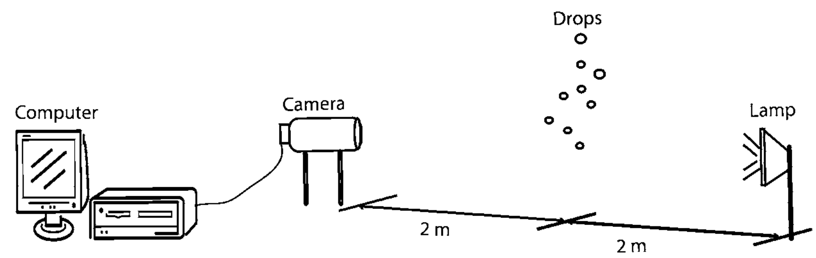

Fig. 1 Raindrop imaging setup.

Generally speaking, the smaller the *dof*, the more accurate is the measured drop size D_m. This is because drops that are closer to (farther from) the camera than the focal point will appear bigger (smaller) than an equivalently sized drop at the focal point. Unfortunately, as for any distribution, attaining a statistically converged measure of the DSD requires a large number of measurements. The number of measurements can be increased simply by recording images for a longer period of time. Because rain storms are of finite duration, and the statistics of raindrops may evolve during the course of a storm, it is desirable to obtain a converged DSD in a relatively short period of time. Hence, a large *dof* is desired because the number of drops that fall between the light source and the camera illustrated in Fig. 1 is finite at a given rain rate. Because *dof* and D_m are effectively determined by the threshold used, the tradeoff between *dof* and measurement accuracy is a function of the thresholding method employed.

Ideally, the threshold used to convert a grayscale image to a binary one is obtained by identifying a minimum in the histogram. This requires a bimodal histogram or at least a histogram with clearly defined minima and maxima. However, the histograms of images obtained from direct optical imaging of raindrops are highly irregular and multimodal. A histogram obtained from a sample raindrop image is presented in Fig. 3, revealing the lack of an easily defined minimum. The process of threshold selection for these complicated histograms becomes easier if the peaks and valleys in the histogram are enhanced to reveal the dominant gray scale levels. Histogram modification techniques are sometimes used to sharpen the peaks for histograms like those in Fig. 3.[14–16] This procedure can follow an iterative or noniterative scheme; however, noniterative techniques require the histogram of the image to be close to bimodal in the first place,[17] suggesting an iterative approach for the present case.

Peleg[14] developed an iterative histogram modification algorithm that reduces the irregularity in the input histogram by reducing the number of nonzero bins to a number small enough to simplify the threshold selection. In Fig. 4, the histogram is presented that is obtained by applying Peleg's algorithm to Fig. 3. The figure shows a significant reduction in the number of nonzero bins.

Peleg's algorithm iteratively sharpens the peaks of a histogram by considering the number of pixels B_i having a particular gray scale level i and comparing it with the average of the number of pixels A in the neighboring R bins on either side of i. Whenever the frequency of the gray scale level under consideration B_i is greater than the average of the number of pixels A, the fraction X is calculated

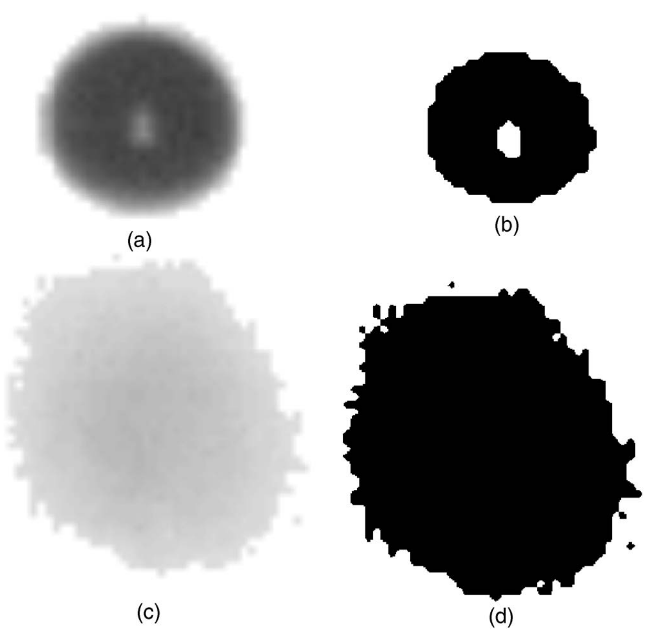

Fig. 2 Sample images of raindrops: (a) in-focus grayscale version, (b) in-focus binary version obtained after thresholding, (c) out-of-focus grayscale version, and (d) out-of-focus binary version.

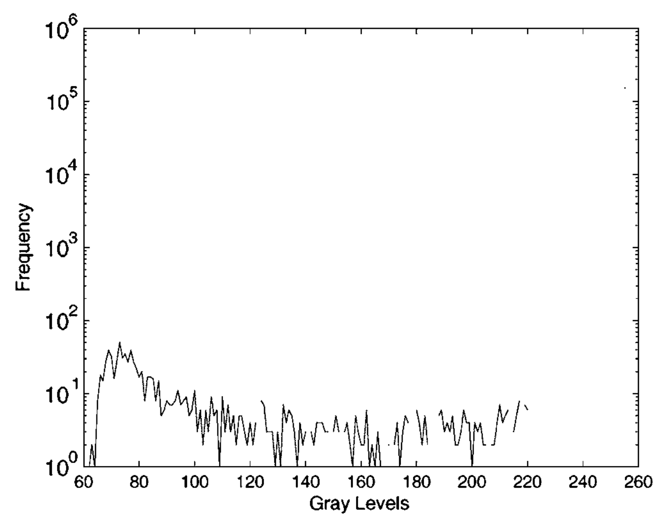

Fig. 3 Sample histogram of a raindrop image obtained using the setup in Fig. 1.

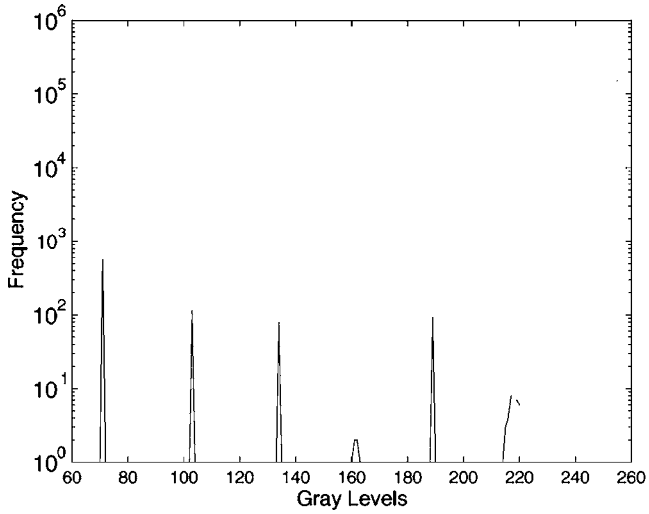

Fig. 4 Histogram obtained after convergence of the Peleg algorithm when applied to the histogram in Fig. 3.

$$X = \frac{(B_i - A)}{B_i}, \tag{4}$$

and this fraction of pixels is shifted from each of the bins in the neighborhood R to their neighboring bin nearest to i. This process is repeated until the histogram of the image converges to a final state. Following the treatment presented by Peleg,[14] the pseudocode is as follows:

```
for n=1,2,3,..., total number of iterations
  {
  for i=1,2,3,..., total number of gray scale levels
    {
    Calculate the average A of the neighboring 2*R bins
    if B_i>A
      {
      X=(B_i-A)/B_i
      for j=R,...,1
        {
        Move B_{i+j}×X pixels from B_{i+j} to B_{i+j-1}
        }
      for j=R,...,1
        {
        Move B_{i-j}×X pixels from B_{i-j} to B_{i-j+1}
        }
      }
    }
  }
```

The original version of the Peleg algorithm described above resulted in images that, when thresholded, gave somewhat rough boundaries for the drop and hole edge. We experimented with altering the Peleg algorithm in an attempt to create smoother boundaries without resorting to a separate smoothing algorithm and found that improvements were obtained by reversing the order in which pixels are moved in the neighborhood R. Specifically, smoother boundaries were obtained by changing the sequence of moving pixels from the outer edge inward (as is the case in Peleg's original approach), to moving pixels from the bin closest to the center bin in the neighborhood and then proceeding outward. This modification is achieved by changing the above algorithm so that the central two loops in the algorithm are changed from "for $j=R,\ldots,1$" to "for $j=1,\ldots,R$." The effect of this change is shown on two example images in Fig. 5. Hereinafter, the "Peleg algorithm" refers to this modification of the original Peleg method. Figure 6 shows the evolution of the histogram of an image for different numbers of iterations using this modified Peleg algorithm.

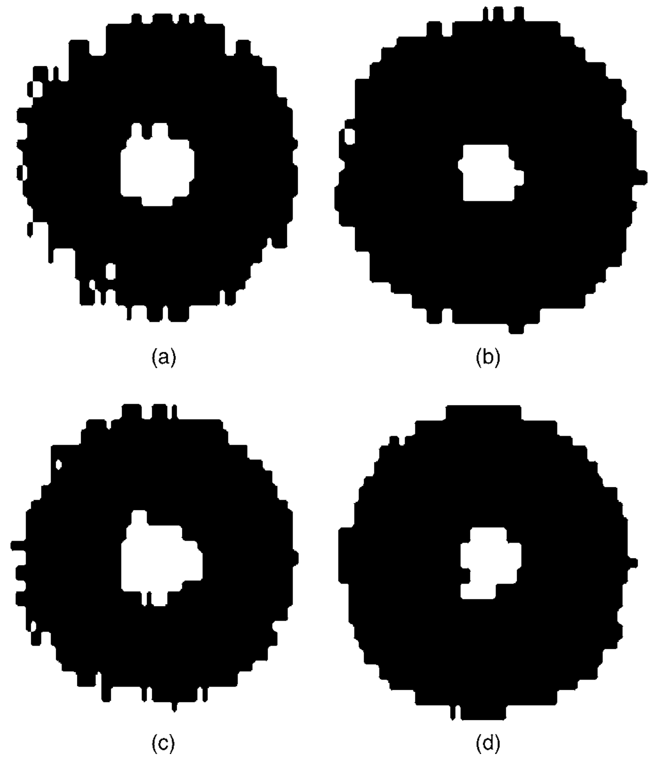

Fig. 5 Sample images showing the performance of the Peleg algorithm and the modified Peleg algorithm. The images on the left were obtained using the Peleg algorithm and those on the right were obtained using the modified Peleg algorithm. For both cases, $R=9$.

We note in passing that Bhattacharya and Yan[18] present a method where the image is divided into subwindows, and then the Peleg algorithm is applied locally to these subwindows. This method tends to preserve the initial appearance of the image and is relevant to images whose histograms are significantly different in different regions of the image. Because the goal of the current study is to process images consisting only of raindrops, characterized essentially by a single histogram, the capability provided by Bhattacharya and Yan[18] is not relevant here.

In the present work, images were collected from the setup shown in Fig. 1 over a large range in z. The Peleg algorithm was applied to each image until convergence in

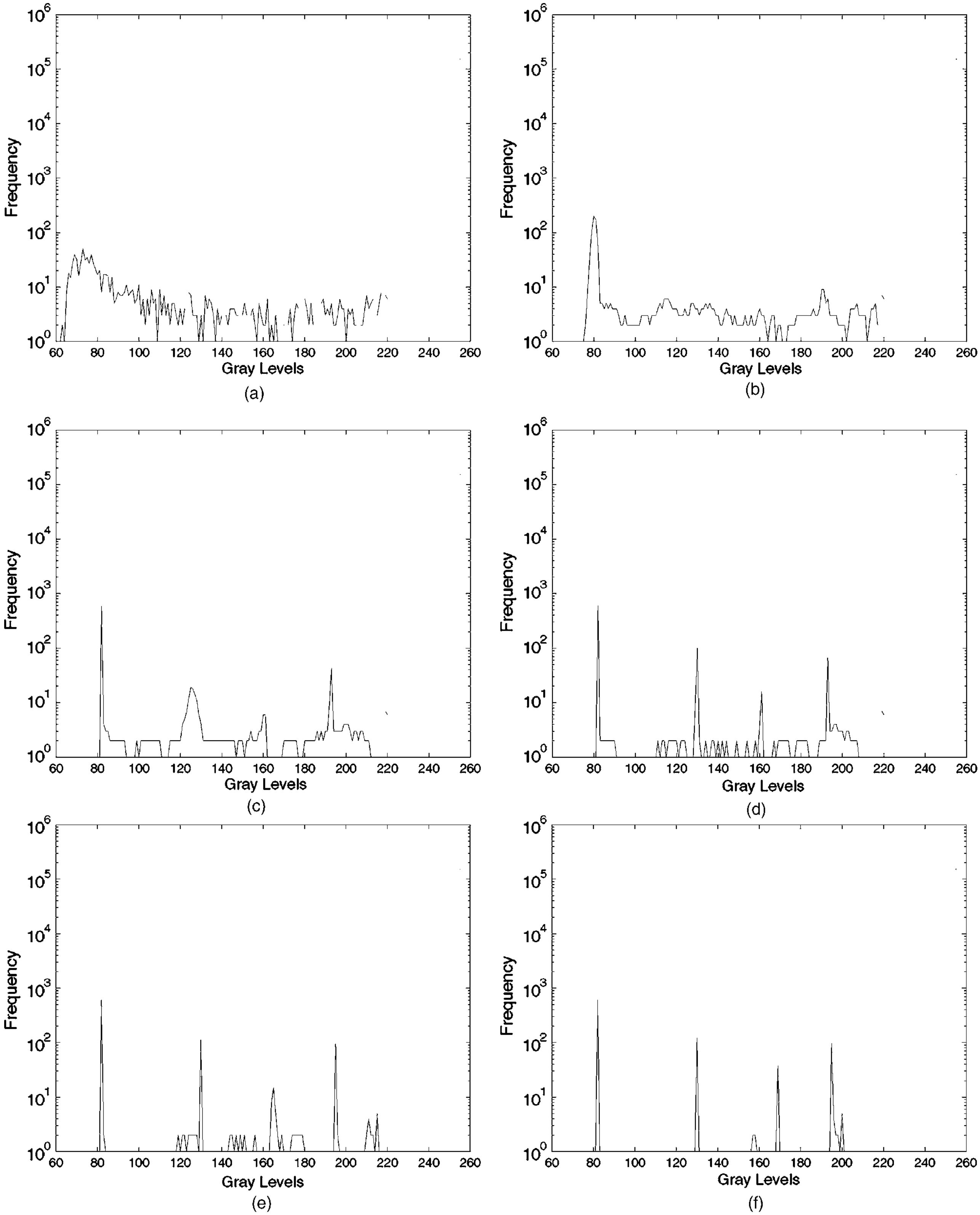

Fig. 6 The histogram of an image at different stages of application of the Peleg algorithm: (a) original histogram, (b) 2 iterations, (c) 5 iterations, (d) 8 iterations, (e) 15 iterations, (f) histogram after convergence (37 iterations).

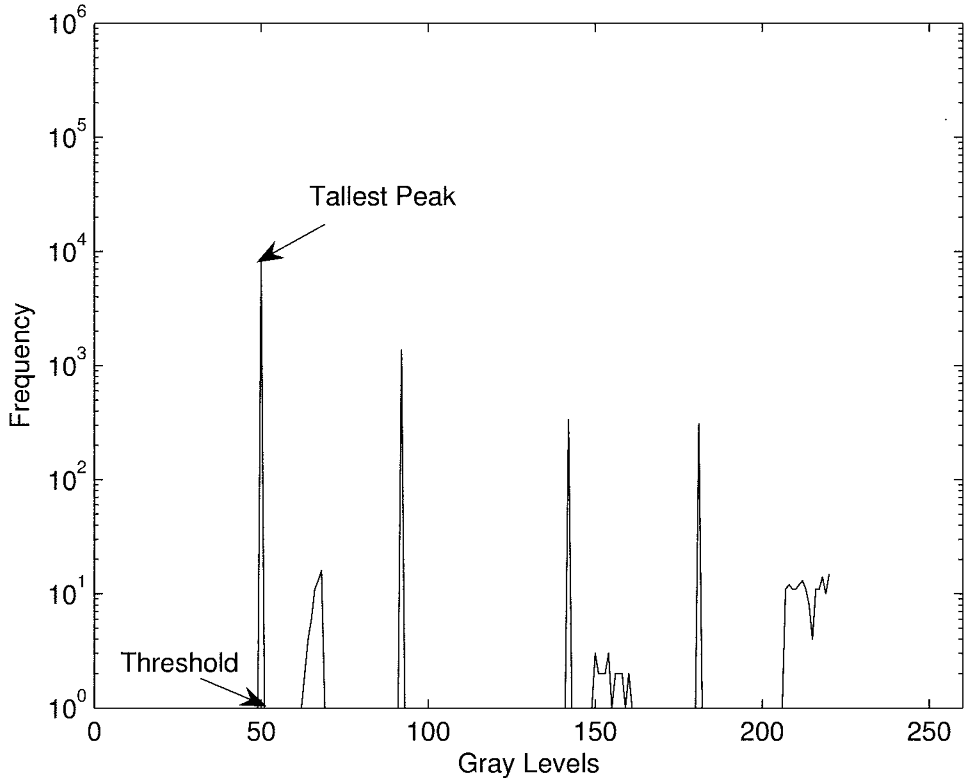

Fig. 7 Final histogram of an image obtained after application of Peleg algorithm illustrating the threshold selection method.

the histogram was achieved. Figure 7 is the converged histogram of a raindrop image. This histogram shows that, although the number of nonzero bins is significantly reduced, even these improved histograms are not bimodal, and hence a method for choosing a threshold is required. By trial and error, it was found that the bin corresponding to the most populated bin in the modified histogram gave the best result in terms of identifying the hole in the image. Figure 7 identifies the threshold value for this particular histogram.

After applying the Peleg algorithm to all of the recorded images, the depth of field and diameter were computed. This process was repeated for two drop sizes and a range of R. The objective of this work is to determine what value of R gives the largest depth of field while accurately measuring the diameter of the drop.

Although the application that we are primarily interested in is raindrop imaging, the measurement of liquid drop sizes is also relevant to several other applications. For example, an understanding of the atomization of fuel into a spray of droplets is critical to combustion processes in engines and gas turbines. In agricultural applications, the efficiency of insecticide and herbicide deposition relies on the characteristics of the liquid spray. The DSDs of paint and coating sprays partially determine the quality of the resulting coating or film. The direct imaging of droplets described herein can be extended to the smaller drop sizes of these industrially relevant sprays, and the image processing algorithms presented herein would extend to such applications as well.

2 Procedure

To achieve the objective of this work, drops having a known diameter were needed so that the measured drop size could be compared to the actual drop size. Because of the practical difficulties associated with consistently producing water drops of a known diameter, magnesium fluoride spheres were used instead of water drops. Magnesium fluoride was chosen because it has a refractive index ($n=1.38$) very close to that of water ($n=1.33$).[19] Figures 8(a) and 8(b) show the grayscale and binary images of an in-focus magnesium fluoride sphere, and Figs. 8(c) and 8(d) show the grayscale and binary images of an out-of-focus sphere.

The experimental setup used to obtain these images was an indoor version of the setup presented in Fig. 1. A personal computer controlled by a LABVIEW code was used to acquire and store images. The setup had a stand, the position of which was varied along the optical axis. This stand consisted of a horizontal extension mounted with a plate having a hole through which the magnesium fluoride spheres were dropped. The stand can be located anywhere within 15 cm on either side of the focal point with a resolution of 1 mm. The stand was moved to positions over a large range of z. At each z location, images were acquired of the sphere as it fell through the field of view of the camera. The size of the image frame was 640×240 pixels. The magnification of the camera was adjusted to obtain a pixel resolution of 0.05 mm/pixel on the x axis and 0.1 mm/pixel on the y axis. The camera lens was set to $f/\#=4.0$, and the camera had an 8-bit dynamic range. Further details of the experimental setup can be found in Saxena and Saylor.[13]

Images were acquired over a 30-cm range of z, centered on the focal point. The images were acquired far from the camera and then progressively inward, crossing the focal point and then continuing closer to the camera. These images were processed, and the z location where processed images started and stopped exhibiting a hole was taken as the starting location z_s and ending location z_e of the *dof*, respectively. Because the volume of data acquired in this laboratory study was not overwhelming, the presence or absence of a hole was determined manually. Images were recorded at finer intervals (1 mm) near the edges of the *dof* to obtain the precise values of z_s and z_e. Images were collected for 3- and 8-mm spheres, and the algorithm was tested on these images for R ranging from 1 to 109. The effect of R on *dof* and D_m was determined. Only images where the drop resided completely within the image frame were considered in this work.

Examination of the binary images obtained using the Peleg algorithm showed that the range of z over which the binary images exhibited a hole was not always continuous. In some cases, a range of z would exhibit a hole in the binary imagery, followed by a small range of z where a hole was not exhibited, followed by another range for which a hole was exhibited. In these situations, the use of Eq. (1) to determine the *dof* would result in inaccuracies. Hence the depth of field for the Peleg algorithm was actually obtained by summing over only those regions where a hole was exhibited

$$dof = \sum_i (z_i - z_p), \tag{5}$$

where z_i is the set of locations where the image of the drop exhibits a hole, and z_p is the location of the image preceding z_i.

Figures 9 and 10 show examples of how the measured diameter varies with z for an 8-mm sphere and a 3-mm sphere, respectively. The vertical lines on each graph show the hole start and the hole end positions. The distance between the two lines is the depth of field. Note that D_m is smaller than D near the start of the *dof* then increases to a value close to D near the focal point and decreases to a smaller value near the end of the *dof*.

An average measured diameter $\langle D \rangle$ was computed to ascertain the performance of the Peleg algorithm for different values of R. As can be seen in Fig. 9, a large z spacing between successive images was used near the center of the *dof*. Due to this unequal z spacing, $\langle D \rangle$ was computed as a weighted average of the measured diameters over the *dof*

$$\langle D \rangle = \frac{\Sigma_i (s_i \times D_{mi})}{dof}, \tag{6}$$

where D_{mi} are the measured diameters obtained at each location i where the image of the drop exhibits a hole, and s_i is the distance between that location and the previous location.

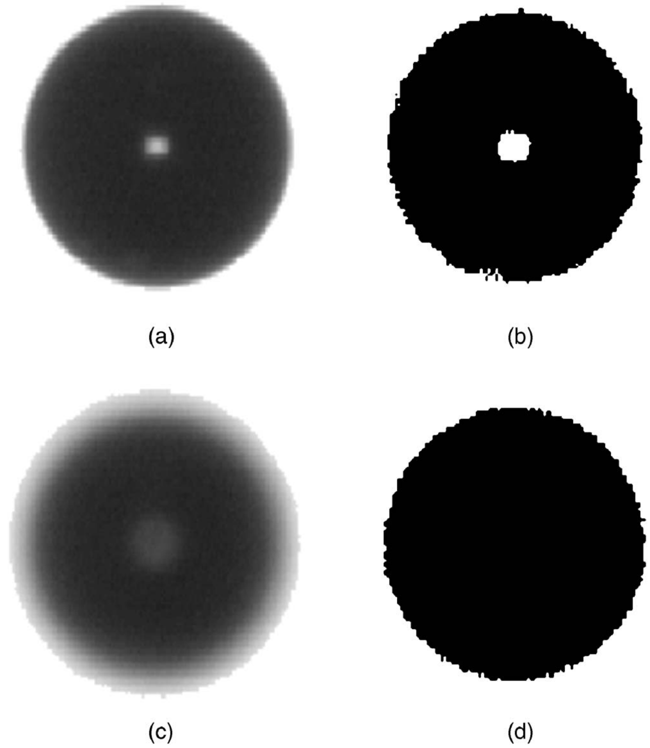

Fig. 8 (a) Sample grayscale image of an in-focus sphere. (b) Binary version of (a) obtained after thresholding. (c) Sample grayscale image of an out-of-focus sphere. (d) Binary version of (c) obtained after thresholding.

3 Results

Figure 11 is a plot of the *dof* versus R for the 8- and 3-mm diameter spheres showing a decrease in *dof* with R. This plot presents *dof* data for $R > 13$ and $R > 9$, respectively. For $R < 13$ for the 8-mm sphere, the *dof* was found to be larger than the current maximum *dof* but the images obtained for these values of R were anomalous and of low quality. An example of such a poor quality binary image is shown in Fig. 12 for $R=1$. Similar imagery was obtained for other neighborhood values in the range $R < 13$, justifying their exclusion. For $R > 75$, the *dof* obtained is very small compared to the *dof* obtained for other R values, and these are also omitted. For similar reasons, the neighborhood range considered for a 3-mm sphere is $R=[9,75]$.

To determine the effect of the neighborhood on the diameter of the drop, the average diameter $\langle D \rangle$ is calculated for each value of R considered. Figure 13 shows the variation of the average diameter with R for an 8- and 3-mm sphere. For both plots, $\langle D \rangle$ increases with R.

4 Discussion

Figures 9 and 10 show that the measured D decreases as one moves away from the focal point (moves toward the edges of the depth of field). This is because the image begins to blur as soon as the drop is moved away from the focal point. The threshold chosen results in a drop boundary that moves in toward the center of the drop as the drop location gets farther from the focal point, regardless of whether the drop is moved closer to the camera, or farther

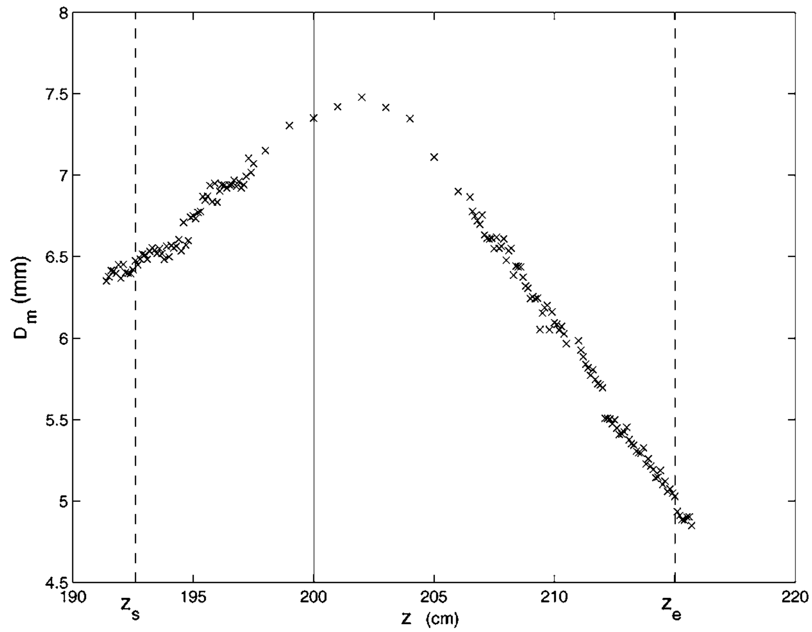

Fig. 9 Plot of D_m versus z for a sphere having D=8 mm. The neighborhood value is R=18. The two vertical dashed lines in this figure indicate where the *dof* begins and ends. The vertical solid line indicates the focal point.

from the camera. The rate of decrease in measured D is approximately the same when moving toward the camera as away from the camera. However, as Figs. 9 and 10 show, the range of z over which a hole is observed in the center of the image is larger when moving away from the camera than when moving toward it. The reason for this is that as one moves away from the camera, one is also moving toward the light source. This results in a greater amount of light collected by the drop (if one thinks of the drop as a lens), and so the spot in the center of the drop image "lasts" longer on this side of the focal point.

Figures 11 and 13 show that *dof* and $\langle D \rangle$ are inversely related, that is, as the *dof* increases the average measured diameter decreases and vice versa. These figures show that if the R value in the region having the largest *dof* is chosen

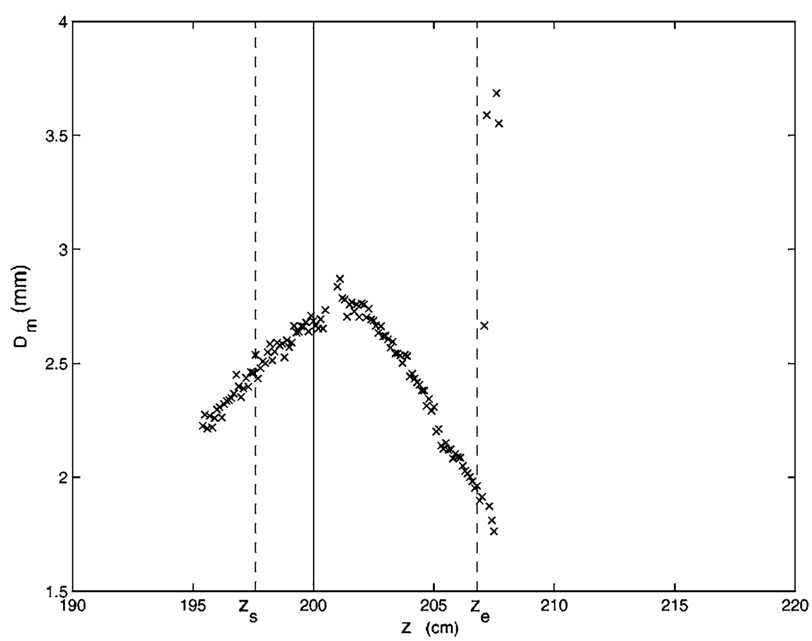

Fig. 10 Plot of D_m versus z for a sphere having D=3 mm. The neighborhood value is R=18. The two vertical dashed lines in this figure indicate where the *dof* begins and ends. The vertical solid line indicates the focal point.

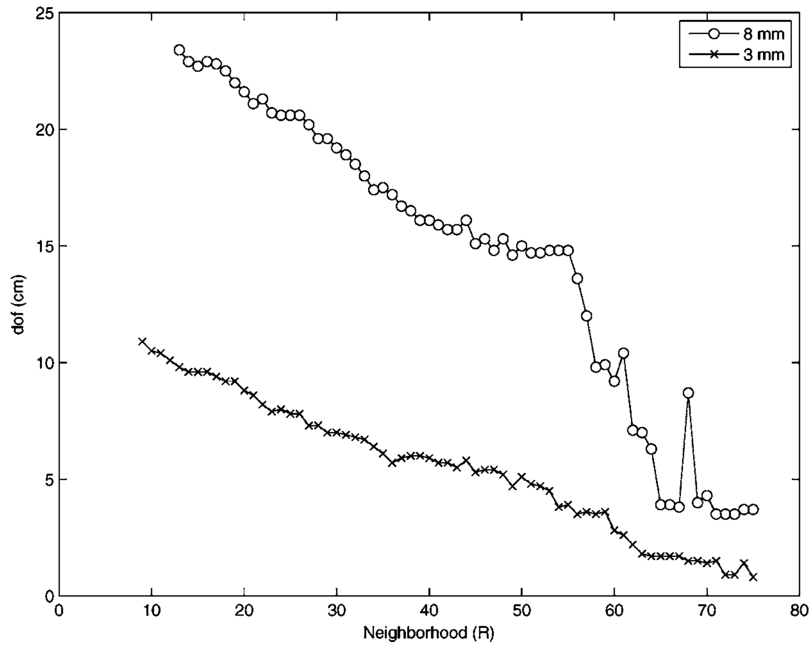

Fig. 11 Plot of depth of field *dof* versus neighborhood size R for spheres with $D=3$ mm (×) and $D=8$ mm (○).

as the optimum R, then a small average diameter results. The variation of the measured diameter with z, discussed in Sec. 2 is responsible for the decrease in $\langle D\rangle$ with increasing *dof*. As the *dof* increases, the number of images obtained at locations far away from the focal point increases, thereby increasing the number of measured diameter values smaller than the actual diameter and this causes $\langle D\rangle$ to decrease from the actual value. Even though the variation of *dof* with R and the variation of $\langle D\rangle$ with R show the same trend for the 8- and the 3-mm spheres, it is found that the trade-offs are not the same for each diameter. So, to obtain the best results, an optimal value of R must be chosen for each diameter.

To evaluate the performance of the Peleg algorithm for different values of R, a figure of merit C was defined

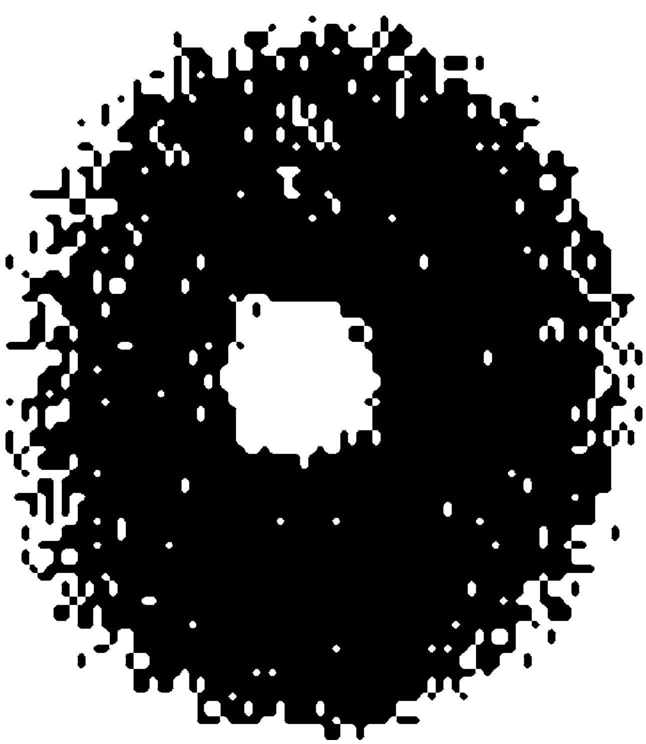

Fig. 12 Poor quality binary image obtained for an 8-mm sphere when using a neighborhood size of $R=1$. The sphere was located at the focal point, $z=200$ cm.

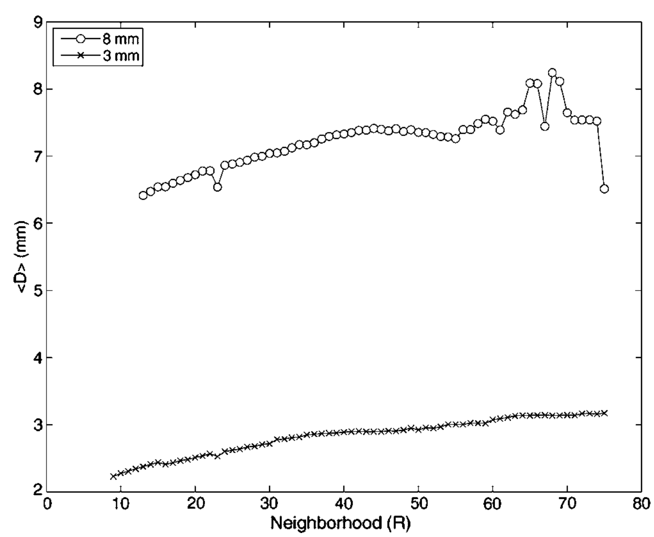

Fig. 13 Plot of the average diameter $\langle D\rangle$ versus neighborhood size R for a sphere with $D=8$ mm.

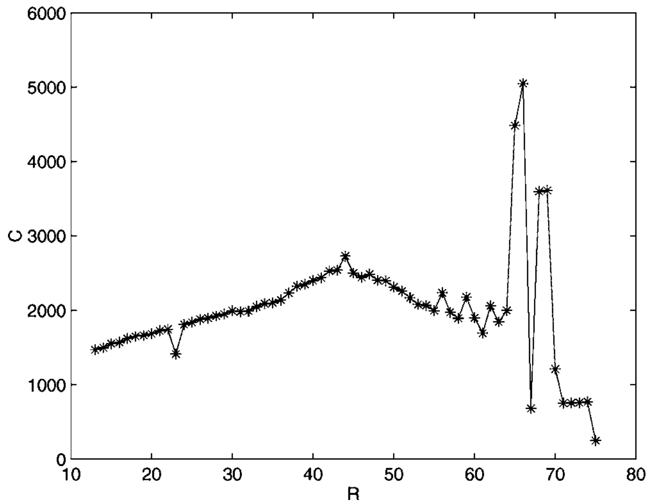

Fig. 14 Plot of C versus neighborhood size R for D=8 mm.

$$C = \frac{dof \times 100}{|\langle D\rangle - D|}. \tag{7}$$

Equation (7) is a ratio of dof to the error in the measured diameter. Plots of C versus R are presented in Figs. 14 and 15. These two figures indicate that the best performance of the Peleg algorithm based on C occurs for R=66 for an 8-mm sphere and R=56 for a 3-mm sphere. Knowledge of the variation of dof with $\langle D\rangle$ provides flexibility in choosing the desired dof within the required accuracy for the diameter. For example, for an 8-mm sphere, if the diameter is to be estimated with the least possible error, then R=70 will give the desired results. On the other hand, if the maximum possible dof is desired, then R=10 should be selected.

From the plot of dof versus R for a 3- and an 8-mm sphere (Fig. 11), it can be seen that the depth of field varies with the size of the drop for a given value of R. For a 3-mm sphere, the dof obtained is smaller than that obtained for an 8-mm drop. This is because the number of pixels in a 3-mm sphere is smaller than that for an 8-mm sphere. That is, as the size of the sphere gets smaller, the size of the hole in the image does as well. Because the smallest hole is 1 pixel in size, a smaller sphere will necessarily have a smaller range of z over which a hole will be observed, namely, a smaller dof.

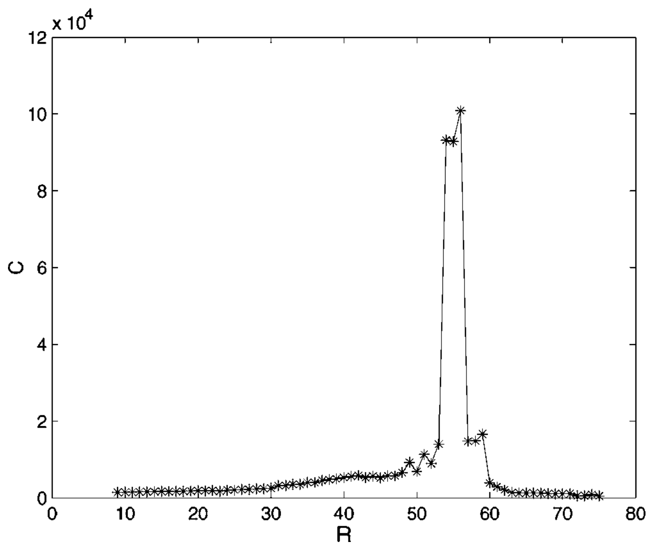

Fig. 15 Plot of C versus neighborhood size R for D=3 mm.

It is noted that in the work presented here, the minimum sphere diameter used was 3 mm, but raindrops can have diameters considerably less than 3 mm. However, by using a higher magnification ratio lens, smaller droplet diameters can be imaged, and hence the only real lower limit to the overall method presented here is the diffraction limit for the wavelength of light used. That is, the performance of the Peleg algorithm presented here should be the same for raindrop images much smaller than the spheres imaged in this work should those images be obtained with a system having a magnification ratio that brings them to a size in pixels comparable to those images presented here.

5 Conclusion

The purpose of the study was to develop a method to obtain measurements of DSDs. To achieve that objective, accurate measurements of the drop size are required along with a large depth of field. From the results obtained from this study, it is seen that there is a trade-off between the two. This is because a larger depth of field results in a larger variation of diameters and thereby reduces the accuracy of the diameters obtained. On the other hand, a smaller depth of field will give more accurate estimates of diameters but this is not of much practical use. Although the Peleg algorithm investigated here does not eliminate this trade-off, it permits the user control over the trade-off via the neighborhood size R.

Acknowledgment

This work was supported by the National Science Foundation Grant no. 0503818.

References

1. R. J. Doviak and D. S. Zrnić, *Doppler Radar and Weather Observations*, Academic Press Inc., Orlando, Fla. (1984).
2. V. N. Bringi and V. Chandrasekar, *Polarimetric Doppler Weather Radar*, Cambridge University Press, Cambridge, UK (2001).
3. P. Meischner, *Weather Radar*, Springer, New York (2004).
4. K. V. Beard, "Oscillation models for predicting raindrop axis and backscatter ratios," *Radio Sci.* **19**, 67–74 (1984).
5. K. V. Beard and C. Chuang, "A new model for the equilibrium shape of raindrops," *J. Atmos. Sci.* **44**, 1509–1524 (1987).
6. K. V. Beard, R. J. Kubesh, and H. T. Ochs, "Laboratory measurements of small raindrop distortion. Part 1: Axis ratios and fall behavior," *J. Atmos. Sci.* **48**, 698–710 (1991).
7. K. V. Beard and R. J. Kubesh, "Laboratory measurements of small raindrop distortion. Part 2: Oscillation frequencies and modes," *J. Atmos. Sci.* **48**, 2245–2264 (1991).
8. K. Andsager, K. V. Beard, and N. F. Laird, "Laboratory measurements of axis ratios for large raindrops," *J. Atmos. Sci.* **56**, 2673–2683 (1999).
9. K. V. Beard and A. Tokay, "A field study of raindrop oscillations: Observations of size spectra and evaluation of oscillation causes," *Geophys. Res. Lett.* **18**, 2257–2260 (1991).
10. J. R. Saylor, B. K. Jones, and L. F. Bliven, "Single-camera method to determine the optical axis position of ellipsoidal drops," *Appl. Opt.* **42**, 972–978 (2003).
11. J. R. Saylor, B. K. Jones, and L. F. Bliven, "A method for increasing depth of field during droplet imaging," *Rev. Sci. Instrum.* **73**, 2422–2427 (2002).

12. L. Bliven, Personal Communication (2001).
13. D. D. Saxena and J. R. Saylor, "Use of thresholding algorithms in the processing of raindrop imagery," *Appl. Opt.* **45**, 2672–2688 (2006).
14. S. Peleg, "Iterative histogram modification, 2," *IEEE Trans. Syst. Man Cybern.* **8**, 555–556 (1978).
15. A. Rosenfeld and L. S. Davis, "Iterative histogram modification," *IEEE Trans. Syst. Man Cybern.* **8**, 300–302 (1978).
16. A. Rosenfeld, "Iterative methods in image analysis," *Pattern Recogn.* **10**, 181–187 (1978).
17. J. S. Weszka, "A survey of threshold selection techniques," *Comput. Graph. Image Process.* **7**, 259–265 (1978).
18. P. Bhattacharya and Y. Yan, "Iterative histogram modification of gray levels," *IEEE Trans. Syst. Man Cybern.* **25**, 521–523 (1995).
19. J. Lucas, F. Smektala, and J. L. Adam, "Fluorine in optics," *J. Fluorine Chem.* **114**, 113–118 (2002).

Nithya A. Sivasubramanian received the BE degree from PSG College of Technology, Coimbatore, India, the MSIE degree from Purdue University, West Lafayette, IN, and the MS degree from Clemson University, Clemson, SC in 2002, 2004 and 2006 respectively.

John R. Saylor received the BS degree from the State University of New York at Buffalo in 1986, the MS degree from the University of Minnesota in 1989 and the PhD degree from Yale University in 1993. He was an NRC Postdoctoral Associate at the Naval Research Laboratory in Washington, D.C. and has been a member of the faculty of the Department of Mechanical Engineering at Clemson University since 2000. Professor Saylor is a member of the American Physical Society, the American Society of Mechanical Engineers, and Sigma Xi.